# Measurement of diagenetic compaction strain from quantitative analysis of fault plane dip

Raluca Cristina Neagu [a,*], Joe Cartwright [a], Richard Davies [b]

[a] 3D Laboratory, School of Earth and Ocean Sciences, Cardiff University, Main Building, Park Place, Cardiff CF10 3YE, UK
[b] Department of Earth Sciences, Durham University, Science Labs, Durham DH13LE, UK

## ARTICLE INFO

## ABSTRACT

We developed a new technique for quantifying the amount of porosity loss during diagenetic transformation of opal-A to opal-CT. The technique is based on 3D seismic data from offshore Norway, where the widely developed biosiliceous sediments of the Brygge Formation are deformed by a polygonal fault system. Evidence is shown from two study areas that the dip of the polygonal fault planes reduces abruptly across the opal-A to opal-CT diagenetic boundary, suggesting that the fault planes were passively rotated into shallower dips due to diagenesis. The reduction of fault plane dip was used to quantify the vertical compaction strain due to diagenesis. Using an independent assessment of the magnitude of the porosity loss, we are able to validate the method based on fault plane dips, and also to evaluate whether the porosity loss results in an exclusively vertical strain. Additionally, the impact of silica diagenesis on the shear strength of the sediments and fault growth is investigated. We present evidence suggesting that deviations from classical Mohr–Coulomb behaviour may be expected during the combined processes of diagenesis and porosity collapse, and may indeed be sufficient to promote continued fault growth.

© 2010 Elsevier Ltd. All rights reserved.

## 1. Introduction

It is well established that listric curvature of fault planes can result from compactional flattening of the fault plane as a passive marker during burial, either during or after the main phase of fault activity (Jones and Addis, 1984; Davison, 1987). This compactional effect may explain at least some of the widely observed listric fault geometries exhibited by normal faults in shallow parts of sedimentary basins (e.g. Shelton, 1984). Compactional flattening of fault planes is likely to be most pronounced where a fault transects a dominantly fine-grained sedimentary succession, because the amount of compaction due to consolidation is much greater for finer-grained than for coarser lithofacies (Rieke and Chilingarian, 1974; Velde, 1996). The quantification of compaction strain is an important element in basin analysis, because it accrues as a result of the advective loss of pore fluid from the originally deposited sediment, and this flux is a critical input into analyses of pore fluid overpressure, fluid flow, and thermal evolution of sedimentary basins (Audet and Fowler, 1992; Bayer and Wetzel, 1989; Bethke and Corbet, 1988).

Based on normal faults from an outcrop in the Recôncavo Basin (NE Brazil), Davison (1987) recognised that the early normal faults in shale act like passive markers subjected to compaction. He suggested that their dip shallows due to compaction and discussed the decompaction of the fault plane dips. The present study takes further his observations, applying them to a much larger scale. In general, small scale methods have been employed to estimate vertical flattening strains, e.g. from the deformation of bedding around nodules (Craig, 1987), or from ptygmatic folding of sandstone dykes (Parize and Beaudoin, 1988). On a slightly larger scale, differential compaction of isolated channel sand bodies encased in a muddier host lithology has also been used to infer vertical flattening strains (Hillier and Cosgrove, 2002). More recently, forward modelling of differential compaction folding due to irregular advancement of a silica diagenetic front has been undertaken to quantify the effects observed during diagenetic transformation of opal-A to opal-CT (Davies, 2005; Meadows and Davies, 2008). This diagenetic transformation involves a relatively sudden loss of a considerable fraction of the porosity, due to mineral dissolution and precipitation over a narrow depth interval of typically a few tens of meters (Isaacs, 1981; Chaika and Dvorkin, 1997; Nobes et al., 1992; Davies et al., 2008).

This paper focuses on the impact of this diagenetically-induced compaction on fault plane dips, where a pre-existing fault is

embedded in a sedimentary succession that is subject to silica diagenesis. The main aims of this paper are to document the nature of the relationship between fault plane dip and porosity loss due to silica diagenesis, and to develop a method for quantifying the amount of porosity loss from measurement of fault plane dip. By attempting an independent assessment of the magnitude of the porosity loss, we are able to validate the method based on fault plane dips, and also to evaluate whether the porosity loss results in an exclusively vertical strain. A purely one-dimensional flattening would be the predicted result for classical models of soil or sediment consolidation (Terzaghi and Peck, 1948; Skempton, 1981), rather than an alternative of a more fully three-dimensional strain, which might be expected for chemical compaction where cementation is a major process for reduction of porosity (Cartwright and Lonergan, 1996).

Our method for estimating the compaction strain during diagenesis is based on observations of fault plane dip using 3D seismic data from the continental margin of Norway, in which widely developed biosiliceous sediments of the Brygge Formation (Brekke, 2000) are deformed by a polygonal fault system. Polygonal fault systems are laterally extensive arrays of extensional faults arranged in polygonal patterns in map view and confined to a specific stratigraphic interval (Cartwright and Dewhurst, 1998). Polygonal faults have been extensively described in recent years based mainly on reflection seismic data (e.g. Henriet et al., 1991; Cartwright, 1994, 1996; Cartwright and Dewhurst, 1998; Dewhurst et al., 1999; Watterson et al., 2000; Goulty, 2001, 2002; Stuevold et al., 2003; Goulty and Swarbrick, 2005), but there has been only limited investigation of the relationship between polygonal faulting and silica diagenesis (R. Davies et al., 1999; Davies, 2005; Davies et al., 2008, 2009), and this has not addressed the question of fault plane dip. We show evidence from two study areas that the dip of the polygonal fault planes reduces abruptly across the opal-A to opal-CT (from here abbreviated A/CT) diagenetic boundary, and a central theme of this paper is that this reduction in dip is due to the diagenetic loss of porosity.

A secondary theme of this paper is the extent of any effect of the silica diagenesis on the shear strength of the sediments and whether, if at all, this impacts fault growth e.g. through changing the physical properties of the deforming sediments. It is pertinent to ask, for example, whether slip accumulation on the faults is reduced or ceases altogether either as a result of the reduction in fault plane dip or due to the change in physical properties once opal-A has been converted into opal-CT. Investigations of the role of diagenesis on the evolution of sediment physical properties during burial and deformation are in their infancy (Shin et al., 2008), so our motivation is that the quantification here of the relationship between fault plane dip and physical property changes due to diagenesis may help promote further research on these complex, coupled phenomena.

Biosiliceous sediment is mainly composed of diatom frustules and radiolarian tests (amorphous silica or opal-A). They are relatively resistant to mechanical compaction, showing a remarkably high retention of porosity during burial (Hamilton, 1976). Opal-A converts to opal-CT (cristobalite and tridymite) by a set of reactions involving dissolution of opal-A and precipitation of opal-CT (e.g. Murata and Larson, 1975; Isaacs, 1981; Williams and Crerar, 1985). The diagenetic transformation occurs at low temperature, generally in the range 20–50 °C the precise value depending on lithology, pH, presence or absence of clays and carbonate, and sediment age (Kastner et al., 1977; Williams and Crerar, 1985). The diagenesis results in a dramatic reduction in porosity (e.g. Chaika and Dvorkin, 2000). Typical ODP (Ocean Drilling Program) boreholes calibrating this diagenetic transformation show ranges from 5 to 25% reduction in porosity values, with the lower values relating to lesser proportions of opal-A in the bulk sediment. In many ODP and industry borehole calibrations, the reduction in porosity occurs over a vertical interval of approximately 10–20 m (e.g. Nobes et al., 1992). It has been shown that this porosity reduction results from diagenesis and not from gradual mechanical compaction due to increasing sediment load (e.g. Isaacs, 1981).

The decrease in porosity during silica diagenesis is correlated to an increase in sediment bulk density and compressional wave velocity (Nobes et al., 1992). Importantly for this study, these changes combine to give a pronounced acoustic impedance contrast and this vertically abrupt contrast ensures a high-amplitude response marking the diagenetic boundary on seismic reflection data (e.g. Hein et al., 1978; Bohrmann et al., 1992; Brekke, 2000; Davies and Cartwright, 2002). Seismic reflection data can thus be used effectively to map the spatial position of the diagenetic front, often over large areas of sedimentary basins (Davies, 2005; Cartwright, 2007).

Davies (2005) has demonstrated that biogenic silica diagenesis can cause enhanced rates of sediment compaction and subsidence in sedimentary basins during early burial. Other authors have investigated the effect of biogenic silica on sediment compaction (Volpi et al., 2003; Davies, 2005; Davies et al., 2008) and porosity reduction during diagenesis (Compton, 1991; Chaika and Dvorkin, 2000; Meadows and Davies, 2008).

## 2. Regional geological setting

This paper is based on results from two study areas (Fig. 1), both located in the Norwegian Sea in a continental margin setting and which developed during three main rifting episodes, in the Permian-Early Triassic, in the Late Jurassic-Early Cretaceous and in the Late Cretaceous-Paleocene (e.g. Brekke and Riis, 1987; Skogseid and Eldholm, 1989; Doré and Lundin, 1996). The rifting culminated in the Late Paleocene–Early Eocene (~55 Ma) with the onset of sea-floor spreading in the North Atlantic (Skogseid et al., 1992; Blystad et al., 1995; Scheck-Wenderoth et al., 2007). The final continental break-up and subsequent thermal subsidence led to the development of the Vøring and Møre sedimentary basins (Brekke, 2000). The basins are filled with more than 10 km of Cretaceous and Cenozoic sediments (Scheck-Wenderoth et al., 2007). Following the onset of sea-floor spreading, the Norwegian Margin was subjected to inversion tectonics during the Neogene, expressed by large-scale domes and elongated anticlines (e.g. Ormen Lange Dome) (Blystad et al., 1995; Doré and Lundin, 1996; Gómez and
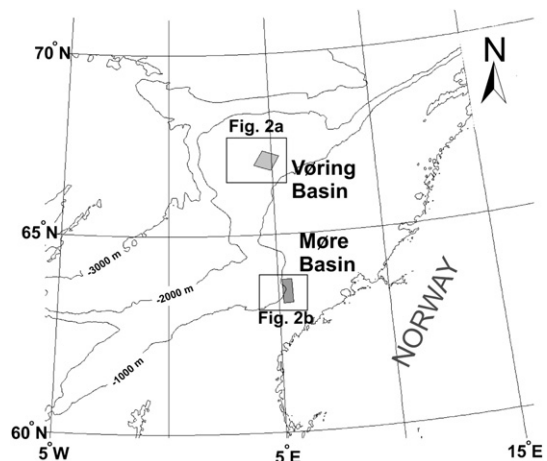


Fig. 1. Map showing the location of the two study areas. Bathymetry from NOAA (Amante and Eakins, 2008).

Vergés, 2005). Both the Vøring and Møre Basins have generally undergone passive subsidence and basinward tilting during the Pliocene to Recent (Brekke, 2000).

The two case study areas are located in areas of active petroleum exploration on the Gjallar Ridge and Ormen Lange Dome (Figs. 1 and 2). These areas and the structures they contain are representative more widely of the relationships observed in the Brygge and Kai Formations throughout the Vøring and Møre Basins.

The main stratigraphic focus of this study is the polygonally faulted Brygge and Kai Formations. The Kai Formation is part of the Nordland Group and is Early Miocene to Late Pliocene in age. It is composed of contourite sediment drifts which developed largely free from the interaction with downslope processes (Bryn et al., 2005) and consists of fine-grained hemipelagic siliceous ooze (Hjelstuen, 1997; Rokoengen, 1995). The Brygge Formation is part of the Hordaland Group and consists of biosiliceous mudstones and claystones (Brekke, 2000). Both the Brygge and Kai Formations have been subject to silica diagenesis (Brekke, 2000; Berndt et al., 2004).

## 3. Data and methodology

The data used in this study consists of two 3D seismic surveys from the two case study areas and well data (ODP Leg 104 Site 642 and two exploration boreholes) (Fig. 2 and Table 1). The seismic surveys cover areas of about 1000 km$^2$ and 1500 km$^2$. The data are zero phased and displayed with positive American polarity equating to positive acoustic impedance contrasts (Brown, 2004). They are time migrated, with a sampling interval of 1 ms and a line spacing of 18.76 m for the Gjallar Ridge survey and 22.79 m for the Ormen Lange survey. The dominant frequency of the data is approximately 45 Hz for the Gjallar Ridge survey and 35 Hz for the Ormen Lange survey. Using an interval velocity of 2000 m/s (Hansen et al., 2005), the vertical resolution is approximately 10 m for Gjallar Ridge, and approximately 13 m for Ormen Lange. The horizontal resolution is equivalent to the bin size and so is approximately 20 m.

Lithological and chronostratigraphic calibration for this study is provided by industry boreholes 6704/12-1 and 6305/5-1 (available from Norwegian Petroleum Directorate, http://www.npd.no), and ODP Leg 104 (Ocean Drilling Program) (Eldholm et al., 1987).

The seismic data were interpreted using GeoFrame interpretational software, to produce a series of maps through the interval of interest (the Brygge and Kai Formations). These maps allowed the definition of faults in this interval, which exhibit the typical characteristics of polygonal fault systems (Cartwright and Dewhurst,

**Table 1**
Interval velocities used for the conversion of the two-way travel time into depth for the two study areas. TVD represents true vertical depth in meters and TWT two-way travel time in milliseconds.

| Survey area | Well | Marker horizons | TVD (m) | TWT (ms) | Interval velocities (m/s) |
|---|---|---|---|---|---|
| Gjallar Ridge | 6704/12-1 | Base Upper Middle Miocene (intra Kai) | 1590 | 2138 | 1640 |
| | | Opal-A/CT | 1745 | 2327 | |
| | | Top Brygge | 1920 | 2512 | 1892 |
| Ormen Lange | 6305/5-1 | Base Naust | 1617 | 1925 | 1854 |
| | | Opal-A/CT | 1910 | 2226 | |
| | | Top Balder | 2294 | 2625 | 1924 |

1998). Dip and amplitude attribute maps were computed from the time structure maps using standard processing techniques (Brown, 2004). The faults could be interpreted on seismic profiles with confidence to a positioning accuracy equivalent to the lateral resolution (20 m), from a series of stacked cutoffs of stratal reflections in both hangingwall and footwall. Imaging of fault cutoffs was consistently excellent throughout both survey areas, and there were no problems with imaging artefacts beneath the fault planes, such as fault shadows.

Based on the dip maps of the reflection from the A/CT boundary (called A/CT reflection from here) (Fig. 3), a series of seismic cross-sectional profiles orthogonal to the fault strike were selected in order to measure the true dip angle of the fault planes (e.g. Fig. 4a). We assume that the faults are predominantly dip-slip (see Cartwright et al., 2003). From the seismic sections we took the TWT value (in ms) of the upper and lower fault tips and of the A/CT reflection and calculated the height of the fault both above and below the A/CT reflection (Fig. 5b). The horizontal distances (in m) between the fault tips and the A/CT reflection location were measured on the basemap (accuracy 0.1 m).

Using the available sonic logs from the commercial wells in the area, we extracted the interval velocities above and below the A/CT reflection (Table 1) and used them for the conversion of the fault height from time (ms) to depth (m). In this way we calculated the dip angle of the faults both above and below the A/CT reflection. Where the fault plane was curved rather than planar, we took several readings at approximately 100 m intervals and used the mean value. This typically involved a variation of <10° and was mainly within the fault plane segment below the A/CT reflection. A variation of ±10% in the interval velocities translates into a variation of ±3° in the resultant calculated dip angles (Table 2).
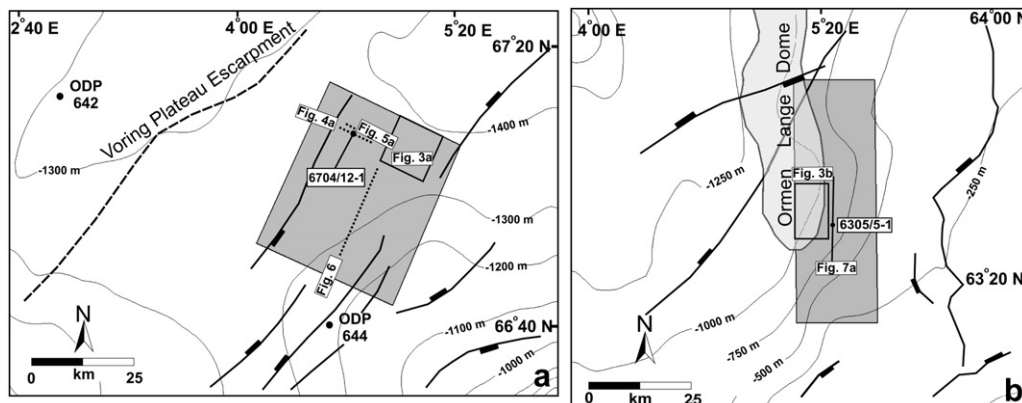


**Fig. 2.** The outline of the 3D surveys (a) Gjallar Ridge; (b) Ormen Lange. The main structural features are from Eldholm (1991) and the bathymetric data from NOAA (Amante and Eakins, 2008). The location of wells 6704/12-1 and 6405/5-1 and ODP sites 644 and 642 are indicated, as well as the location of Figs. 3–7.
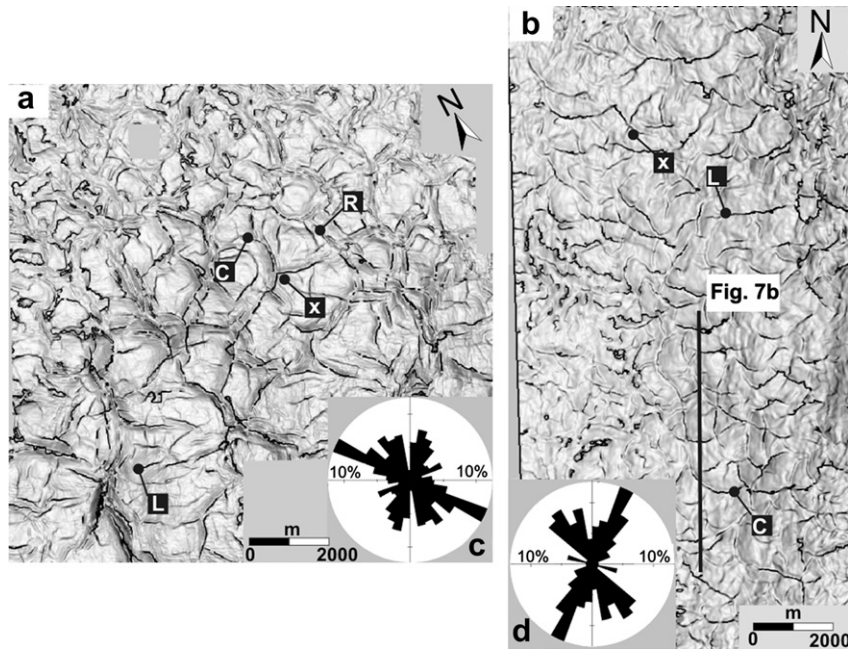
**Fig. 3.** Representative examples of dip maps of the reflection corresponding to the opal-A/opal-CT diagenetic boundary for (a) Gjallar Ridge and (b) Ormen Lange. Dark grey to black regions mark polygonal faults. Examples of curved, linear and radial fault traces are marked with "C", "L" and "R" respectively. "X" marks examples of orthogonal fault trace intersections. Location of Fig. 7b also shown. Rose diagrams representing the strike of the all the measured polygonal faults in (c) Gjallar Ridge and (d) Ormen Lange study areas.

Throw values of selected faults were measured on seismic profiles oriented orthogonally with respect to the fault strike by taking the two-way travel time of reflections from the footwall and hangingwall cutoffs of selected horizons. Typically 10–15 horizons were mapped and thus provide the cutoff positions for these throw measurements for each fault. It should be noted that the throw value corresponding to the A/CT is not the true stratigraphic throw at that point, but the throw on the A/CT reflection.

The throw values were plotted versus two-way travel time (expressed in ms TWT) rather than in true depth (c.f. the $T–z$ plots of Cartwright et al., 1998; Baudon and Cartwright, 2008) (e.g.

Fig. 5c). To check if the depth conversion would result into a different pattern of vertical throw variation, we used the interval velocities (Table 1) for the depth conversion of the $T–z$ profile of fault 97, located nearby well 6704/12-1 in the Gjallar Ridge survey. As presented in Fig. 5c the depth and time profiles have similar patterns; hence the throw versus travel time plot is a reasonable proxy for a $T–z$ plot in this area.

Possible errors of measurement related to drag folding (e.g. Walsh and Watterson, 1987; Mansfield and Cartwright, 1996) were minimised by not including the drag displacement in the throw measurement. The measurement precision is related to the sample
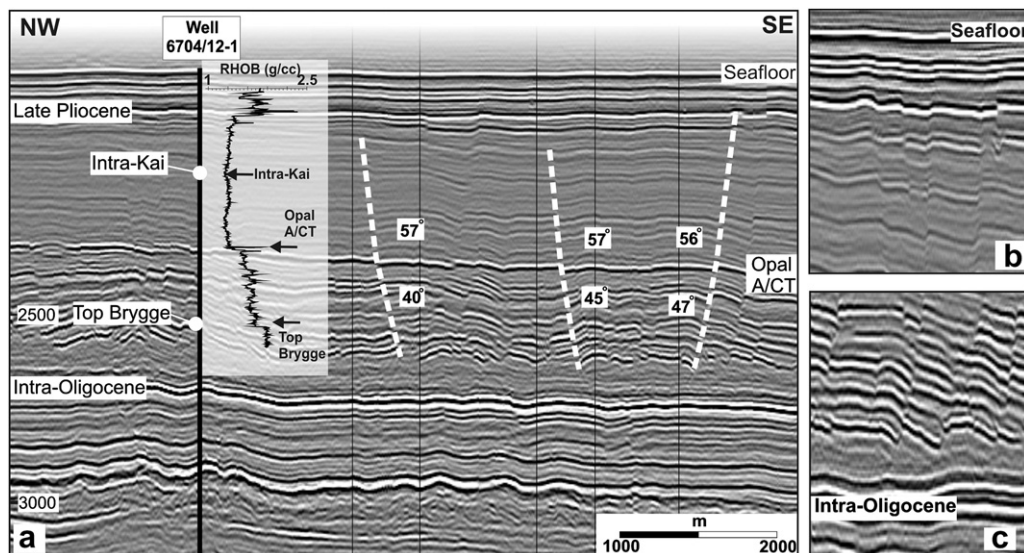


**Fig. 4.** (a) Composite seismic cross-section from the Gjallar Ridge (location in Fig. 2a). The vertical axis represents two-way travel time in milliseconds. The location of well 6704/12-1 and the corresponding density (RHOB) log are also shown. The fault planes are marked with white dashed lines. Note the change in fault dip at the level of the opal-A/opal-CT reflection. The seismic cross-sectional profile is orthogonal to each of the fault strikes. (b) Close-up of the upper tips of the polygonal faults characterised by monoclinal tip folds. (c) Close-up of the lower tip region of the polygonal faults located in a sediment package characterised by low seismic amplitude.
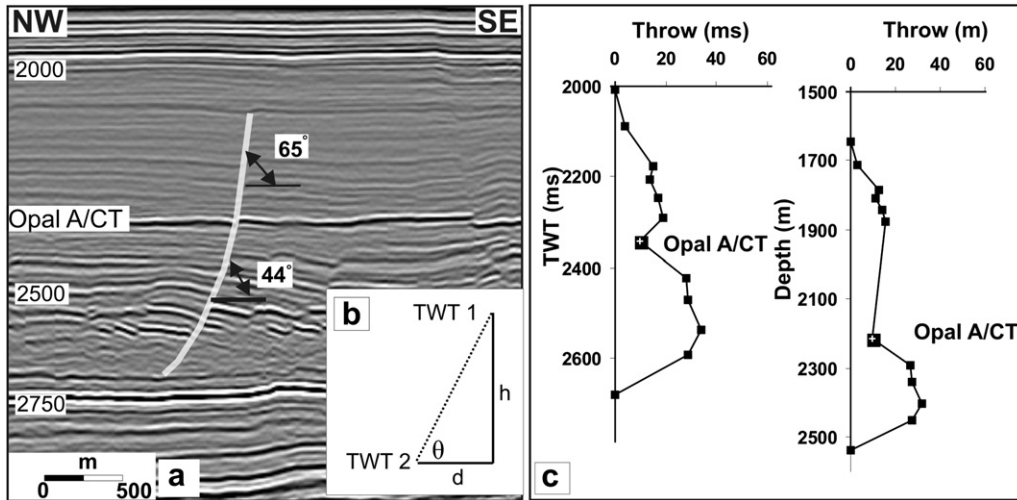
**Fig. 5.** (a) Seismic cross-section orthogonal to the strike of the fault 97 located nearby well 6704/12-1 (location in Fig. 2a). The two-way travel time is in milliseconds. The change in fault dip corresponds to the A/CT reflection. (b) Schematic representation of the method of measurement of the dip angle on the seismic cross-section. Explanation of symbols is: $\theta$ – dip angle of the fault segment (either above or below the A/CT); $h$ – height of the fault computed by subtracting TWT 1 from TWT 2 (in milliseconds); $d$ – horizontal distance (in meters) measured on basemap. (c) Vertical throw distribution plot for Fault 97 representing the throw value in milliseconds plotted against two-way travel time and the same $T$–$z$ profile depth-converted using interval velocities from well 6704/12-1. Note that the throw value corresponding to the A/CT is not the true stratigraphic throw at that point, but the throw on the A/CT reflection.

rate of the seismic data ($\pm$1 ms), the resolution of the seismic data (see for details/description Baudon and Cartwright, 2008) and to the accuracy of the cursor positioning on the screen ($\pm$1 ms); we estimate that the measurement precision is $\pm$2 ms.

## 4. Structural analysis

The description of the main structures in the study areas is followed by a detailed analysis of the geometry of the polygonal faults and the morphology of the A/CT reflection for the two study areas. The structural analysis is based on seismic cross-sections (Figs. 4a and 5a) and dip maps of the A/CT reflection (Fig. 3).

### 4.1. Gjallar Ridge case study

The case study is located on the Gjallar Ridge which in turn is part of the Vøring Basin and consists of a NE trending system of deeply eroded, rotated fault blocks that mainly involve pre-Tertiary sequences (Blystad et al., 1995). Hansen et al. (2005) recognised two structural elements in the Tertiary of the Gjallar Ridge study area: (1) deep-seated faults and flexures and (2) polygonal fault systems. The former are considered to be the uppermost parts of faults and anticlines associated with the deeper seated faults in the underlying Late Cretaceous succession. The polygonal faults are layer bound i.e. they are developed entirely within the Kai and Brygge Formations, deforming slope to basinal sediments of Oligocene to Pliocene age (Fig. 4a). They are part of a basin-wide polygonal fault system that is confined to this stratigraphic interval (Cartwright and Dewhurst, 1998; Brekke, 2000; Berndt et al., 2003) that consists exclusively of small normal faults (throws of up to 70–80 m). In some areas, they have been reactivated in the

Pleistocene to Holocene, possibly by loading under rapid sedimentation (Gay and Berndt, 2007).

Within the survey area, a pronounced seismic reflection with a strong positive polarity (positive acoustic impedance contrast) is calibrated by well 6704/12-1 as being derived from the A/CT boundary. The boundary is set within Early Miocene sediments of the Kai Formation, and is clearly crosscut and offset by a set of polygonal faults (Figs. 4a and 5a).

The A/CT reflection is concordant to the stratigraphy in some areas (Fig. 4a), but it is more typically discordant (Fig. 6) It crosscuts the stratigraphy across regions that are most deformed by the latest phase of the Neogene inversion-related folding (c.f. Davies and Cartwright, 2002). The A/CT reflection is clearly not parallel to the present-day seabed and is therefore not in equilibrium with the present-day thermal regime. Instead it appears to be most parallel

**Table 2**
Interval velocities from Table 1 varied by $\pm$10%.

| Survey area | Well | Interval velocity above A/CT (m/s) | | Interval velocity below A/CT (m/s) | |
|---|---|---|---|---|---|
| | | Min | Max | Min | Max |
| Gjallar Ridge | 6704/12-1 | 1476 | 1804 | 1703 | 2081 |
| Ormen Lange | 6305/5-1 | 1668 | 2040 | 1732 | 2117 |
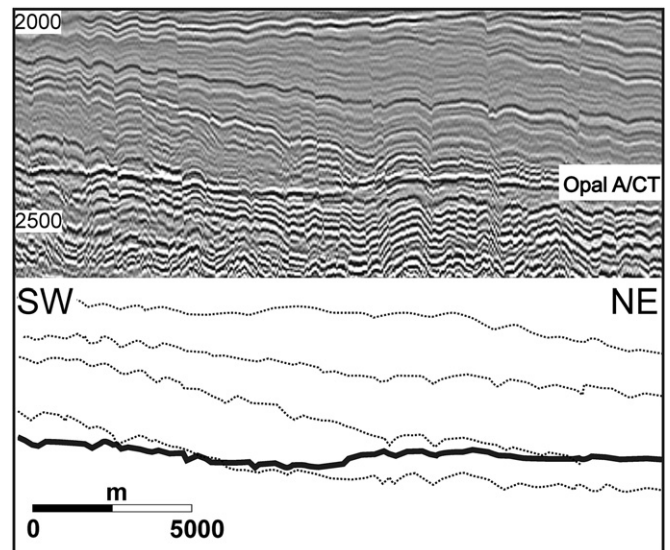


**Fig. 6.** A seismic cross-section (location in Fig. 2a) and associated line-drawing showing the A/CT reflection discordant to the host stratigraphy.

to the reflections in the Kai Formation just below the Late Pliocene unconformity (Fig. 4a), suggesting that the boundary has been fixed in this position from this time onward, as previously suggested by Brekke (2000).

Importantly, the magnitude of the throw of the polygonal faults measured at the A/CT reflection is less than the true stratigraphic throw at that position (Fig. 5c). The A/CT reflection separates two intervals of the faulted tier that are characterised by different gross seismic amplitudes. The lower interval has high seismic amplitudes compared to the upper interval, presumably due to the diagenesis of the opal-A in the mudstones to opal-CT (Davies and Cartwright, 2007). A similar amplitude response has been observed in neighbouring basins along this continental margin (Davies and Cartwright, 2002).

The vast majority of the faults in this area (>90%) do not propagate above the Late Pliocene unconformity, suggesting that they have been inactive since this time. The upper tips of the faults can be clearly identified in most cases: they terminate at different stratigraphic intervals within the Kai Formation, but are usually located at about 250–300 ms TWT below the sea-floor (approximately 200–240 m). Growth packages have only been identified at the upper tips of the largest faults. The upper tips (Fig. 4b) are more generally characterised by monoclinal tip folds typical of upper tips of small blind normal faults observed elsewhere (c.f. Baudon and Cartwright, 2008). The lower tip regions of the faults are located in a package of the Brygge Formation characterised by low seismic amplitude (Intra-Oligocene on Fig. 4c), and it is unclear whether there are local detachments at this level or whether the lower tips terminate against the underlying unfaulted Oligocene units.

Many of the polygonal faults exhibit an unusual, bimodal planar cross-sectional geometry, with two contiguous planar segments with contrasting dip magnitudes. The relatively abrupt change of dip magnitude occurs at or close to the position of the A/CT reflection, with a steeper fault segment above the A/CT reflection compared to that below it (e.g. Fig. 5a). A small number of faults are limited to the upper part of the deformed interval i.e. above the A/CT reflection and these are universally planar. There is no preferential orientation of the fault dip or throw direction, as can be seen, for example, from the seismic profile presented in Fig. 4a.

The regional distribution and planform pattern of the polygonal faults is illustrated with the dip attribute map of the A/CT reflection in Fig. 3a. The dip map shows a uniform distribution of the faults over the area. Most of the fault segments are between 1 and 2 km in length, and are mainly linear (e.g. fault marked 'L' in Fig. 3a), with only a small proportion that are curved in planview (e.g. fault marked 'C' in Fig. 3a). The planform is polygonal and most fault intersections are orthogonal or at a high angle, as is typical of many polygonal fault systems (Lonergan et al., 1998; Cartwright et al., 2003). Some faults (e.g. fault marked 'R' in Fig. 3a) have a radial distribution pattern: they are correlated with deep-seated basement faults and mud diapirs (Hansen et al., 2005). Fault strikes show more than one set of preferred orientations (Fig. 3c), oriented WNW–ESE, NE–SW and SW–NE.

### 4.2. Ormen Lange

The second case study is located on the Ormen Lange Dome, one of the major inversion structures in the Møre Basin (Fig. 1) resulting from the Neogene phase of regional inversion tectonics that affected the entire margin (Doré and Lundin, 1996; Brekke, 2000). This structure has a wavelength of the order of approximately 20–30 km and is elongated with a N–S trending axis. It is underlain by extensional faults that were mainly active during the Late Jurassic, but were reactivated during the Eocene to Miocene inversion (Stuevold et al., 2003).

The A/CT diagenetic transformation is sharply expressed on the seismic data as a high-amplitude positive reflection, calibrated in four wells in or close to the study area, and hosted within the biosiliceous mudstones of the Kai and Brygge Formations (Fig. 7a). The biosiliceous mudstones of the Brygge Formation are characterised by high seismic amplitudes and partly host the polygonal fault system. The tier of polygonal faults is bounded above by the top of the Kai Formation and below by the Top Balder marker, which corresponds to the early Eocene (Stuevold et al., 2003) (Fig. 7a).

The distribution and geometrical characteristics of the polygonal faults is illustrated with the dip map of the A/CT reflection (Fig. 3b). The areal distribution of the faults is fairly uniform (Fig. 3b), with the exception of the western edge of the survey, where the fault density seems to decrease. The fault network consists of large (1.5–2 km long) and small (less than 700 m) fault segments, with orthogonal to high angle intersections (Fig. 3b). There is a high proportion of curved fault segments, with several preferred orientation of the fault traces (Fig. 3d), oriented in the directions NE–SW and SE–NW.

The majority of the polygonal faults that transect the A/CT reflection have a crudely step-like cross-sectional geometry with steeper segments above the A/CT reflection than those below, similar in general shape to the faults in the Gjallar Ridge case study. The fault dip changes abruptly at or close to the A/CT reflection. The faults range from 630 to 720 m in height and have a uniform strike distribution, both in the interval above and below the A/CT reflection. The majority of faults dip upslope (Fig. 7a), a common feature of polygonal fault systems elsewhere (Cartwright, 1994; Goulty and Swarbrick, 2005).

The lower tips of the faults are located in a low amplitude reflection interval, thus their exact geometry cannot be interpreted from the seismic data. The upper tips of the faults terminate within a narrow interval towards the top of the Kai Formation. They are characterised by tipline folds (monoclinal), with no obvious growth packages in their hangingwalls. The maximum throw values are in the range of 17–68 ms TWT, and are usually located in the interval below the A/CT reflection, but there are some exceptions.

### 4.3. Vertical variation in throw on the polygonal faults

In addition to the general observation of the abrupt change of dip at the A/CT reflection in both survey areas, it was also generally observed that the throw values at the level of the A/CT boundary are always smaller than the throw of stratal reflections at the same position on the fault. This latter observation has been made previously in other areas along this margin of the NE Atlantic, and has been attributed to the arrest of the upward migration of the diagenetic front prior to the last period of movement on the polygonal faults (Cartwright, 2007).

In order to quantify this relationship in more detail, vertical throw distributions were measured for 40 representative faults (of which 20 examples are shown in Fig. 8) from the two case study areas. The results were plotted as throw versus travel time ($T$–'$z$') plots. These plots were all constructed through the maximum throw position of each fault and show that the maximum throw measured at the A/CT reflection ranges from a few ms (2–3 m) up to approximately 30 ms (25 m) (Figs. 5c, 7c and 8). In contrast, the stratigraphic throw at the equivalent position on the measured faults ranges from 10 to 70 ms (approximately 8–62 m) (mean value 31 ms). The effect of this reduction is to produce a local minimum at the position of the A/CT reflection that obviously departs from the general pattern of throw on the true stratigraphic markers (Fig. 8). The maximum throw values occur both in the
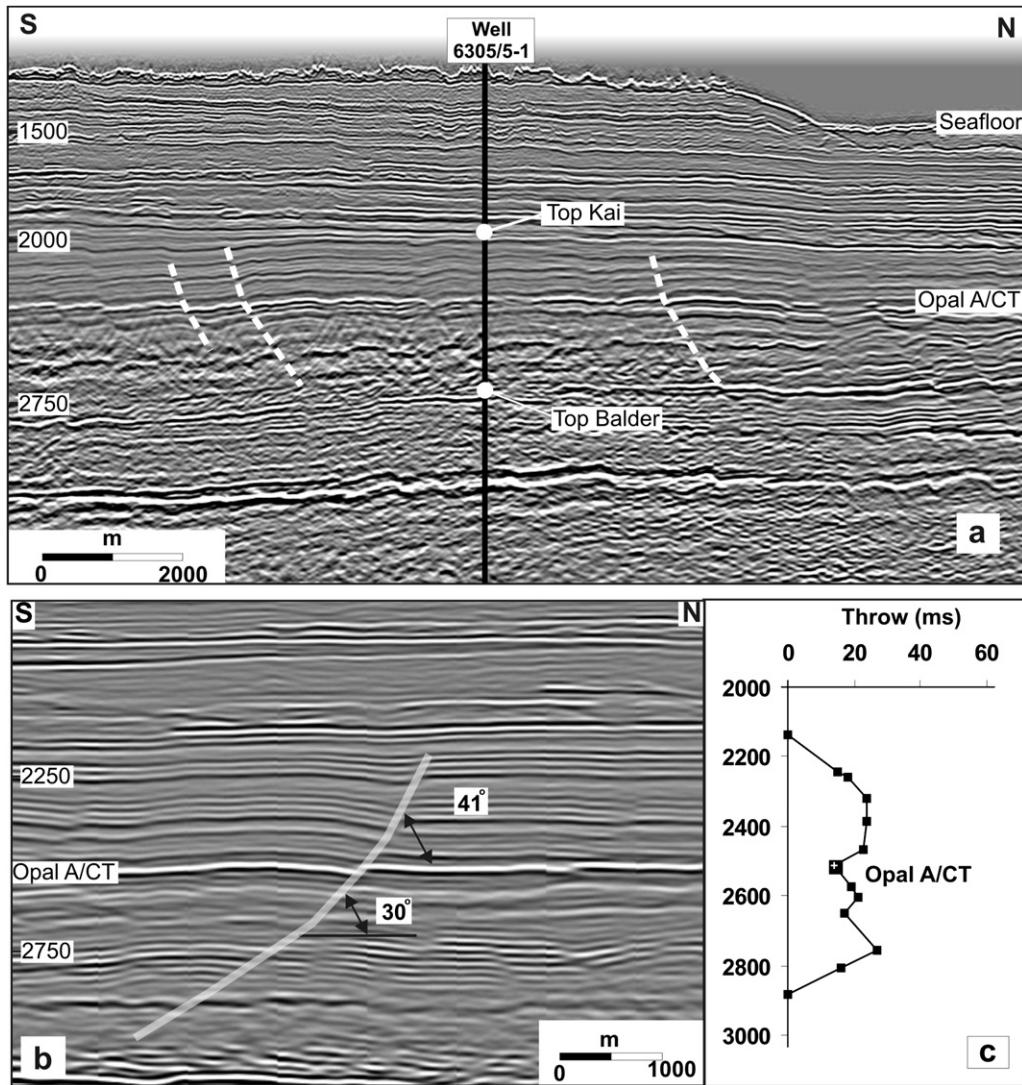
**Fig. 7.** (a) Seismic cross-section from the Ormen Lange survey (location in Fig. 3c). The vertical axis represents two-way travel time in milliseconds. The location of well 6405/5-1 is shown. Several fault planes are marked with dashed white lines. (b) Seismic cross-section orthogonal to the strike of Fault 24 (location in Fig. 3b). The two-way travel time is in milliseconds. The change in fault dip corresponds to the A/CT reflection. (c) Vertical throw distribution plot for Fault 24 representing the throw value in milliseconds plotted against two-way travel time in milliseconds.

interval above the A/CT position (e.g. faults 129, 344 in Fig. 8) and in the interval below it (e. g. fault 8, 87, 68 in Fig. 8).

In general, the vertical throw profiles for the 40 faults are not strictly similar to the C-type or M-type (e.g. Muraoka and Kamata, 1983; Baudon and Cartwright, 2008), but exhibit elements of both types of end member profiles. The C-type is characterised by a symmetrical shape with a gentle change of displacement with depth, while the M-type has a broad central section with no significant change of slope, and adjacent segments with an abrupt change of displacement. A good example of a C-type is fault 129 (Fig. 8), and an M-type is fault 246 (Fig. 8). Strongly asymmetric profiles are common, with approximately 40% of the faults exhibiting a pronounced maximum below the A/CT reflection and within 200–300 m of the basal tip (e.g. faults 5, 68, and 301 in Fig. 8). The asymmetric profiles tend to be those whose faults transect the entire tier. The vertical variation in throw is reasonably smooth, with the exception of the region at or close to the A/CT reflection (Fig. 8).

These throw profiles show conclusively that there is a significant local minimum at the level of the A/CT reflection. They also show

that a substantial proportion (quantified in Appendix 1) of the total throw of each fault accrued on the fault surfaces after upward migration of the A/CT diagenetic front had effectively ceased (Brekke, 2000; Cartwright, 2007). This raises the interesting question of whether the arrest of upward migration of the front, implies that all silica diagenesis had ceased in the interval below the diagenetic front. This question is important because in all the measured cases, especially the case of the highly asymmetric throw profiles-asymmetry that could be explained by a partial slip along the fault-it is evident that in this post-'arrest' phase of fault growth, throw actively accumulated above and below the position of the A/CT reflection.

## 5. Fault plane dip

One of the more important observations noted in the previous section regarding fault plane dip is the abrupt reduction of dip of the polygonal fault planes that occurs at the A/CT boundary (Figs. 4, 5 and 7). This was observed systematically throughout the two seismic surveys presented in this paper, and has also been observed
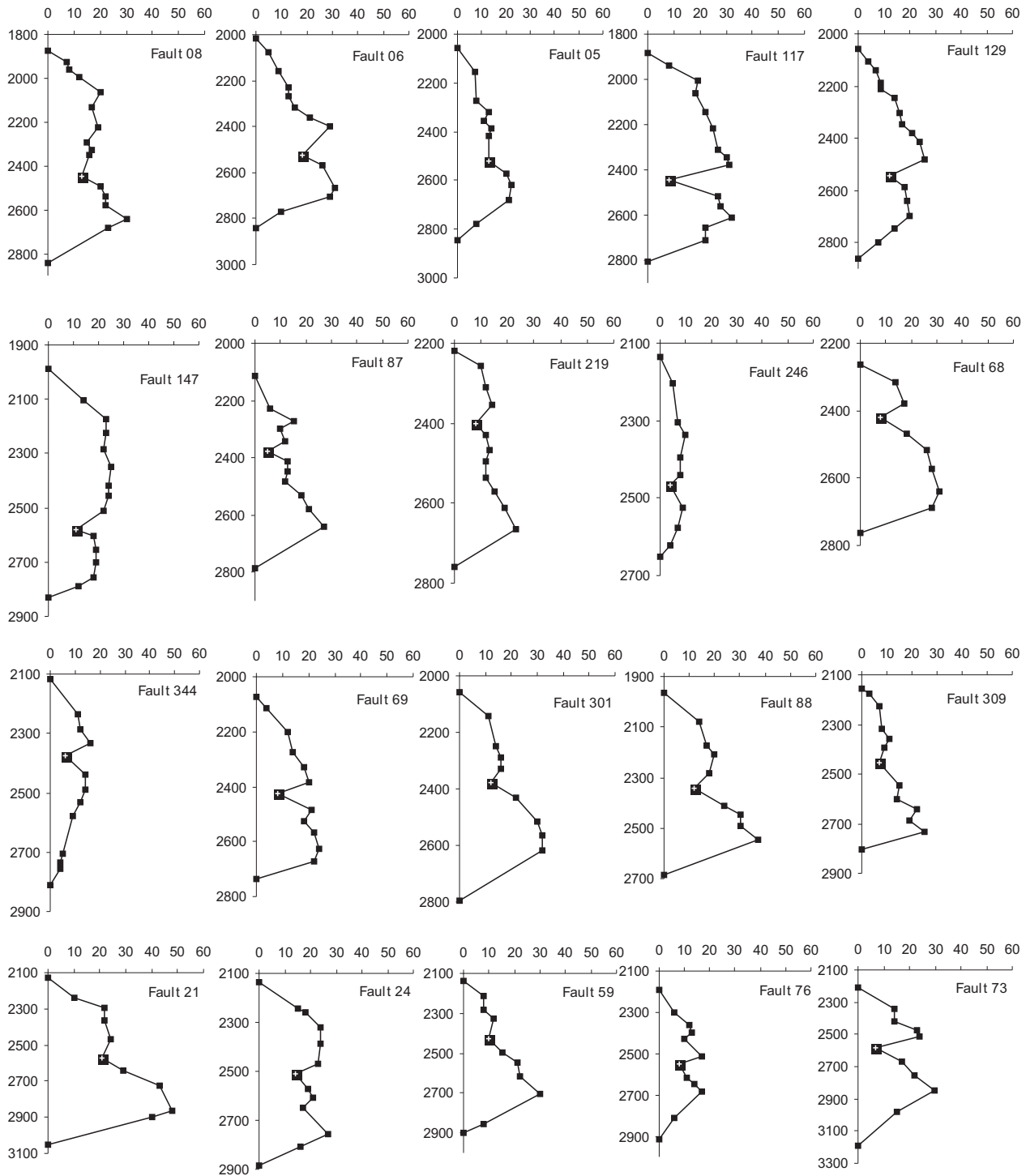
**Fig. 8.** Vertical throw distribution plots for 20 selected faults from both case study areas. The plots from the upper 3 rows correspond to faults selected from the Gjallar survey and the plots from the lowest row to faults from Ormen Lange survey. The throw values are expressed in milliseconds and are plotted against two-way travel time (milliseconds). The throw values at the level of the A/CT reflection are marked by a larger symbol (black square with a white cross). Note the significant local minimum throw values at this level.

on a number of other 3D seismic surveys distributed more widely in the Møre and Vøring Basins.

To evaluate the significance of this abrupt change, we measured the dip angle of 487 fault planes from the two seismic surveys. The results are presented in Fig. 9a for the fault plane segments above the A/CT boundary (dip 'a') and for those below the A/CT boundary (dip 'b'). The histogram (Fig. 9b) and crossplot of 'a' versus 'b' (Fig. 9c) both illustrate that there is a large scatter of dip values for

both upper and lower segments. The dip 'a' values range from 28° to 73°, and the dip 'b' values range from 19° to 57°. The ranges and average values for the individual case studies are presented in Table 3, where it can be seen that the ranges for individual survey areas are less than the total range. An important conclusion from this data is that the dip 'a' value is greater than the dip 'b' in 94% of the cases and of equal value in the remaining 31 faults (to within 2°). This is most clearly illustrated on the crossplots of dip 'a' versus
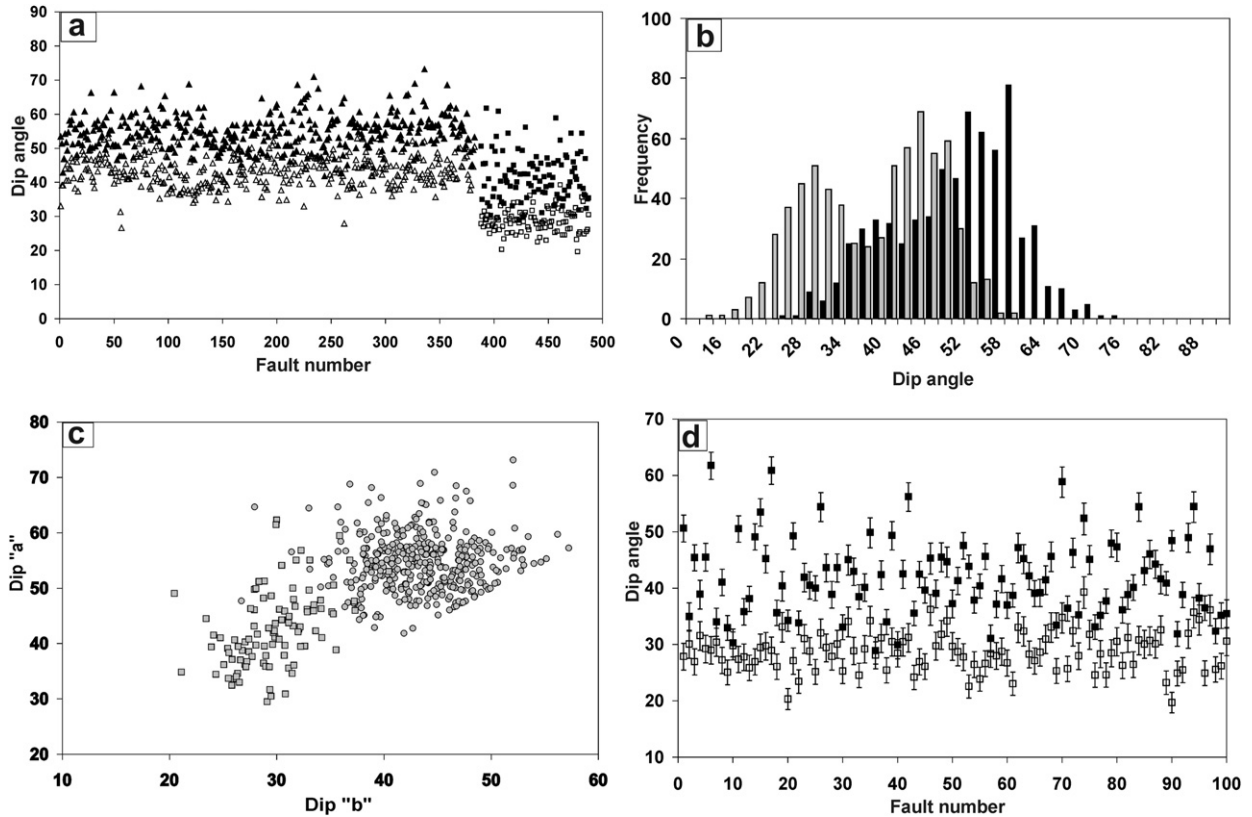
**Fig. 9.** (a) The values of the dip angles of the selected faults in the two surveys (triangles-Gjallar Ridge, squares-Ormen Lange). The dips of the fault segments located within the opal-A rich sediment (dip "a") are marked with filled symbols, while the dips of the fault segments located within the opal-CT rich sediment (dip "b") are marked with open symbols. The ranges of values are presented in Table 3. (b) Histogram showing the frequency of the "a" dip angles (black bars) and "b" dip angles (grey bars). (c) Crossplot of dip "a" versus dip "b" values (grey squares-Ormen Lange data; grey circles-Gjallar Ridge data). (d) Dip angles of the faults in the Ormen Lange survey (filled symbols represent dip "a" and open symbols dip "b") with the associated error bars corresponding to a variation of ±10% of the interval velocity used for the depth conversion (Table 2).

dip 'b' (Fig. 9c). Within error, the dip of the lower segment is never found to be larger than that in the upper segment. The range of fault dips of both the upper and lower segments is clearly much greater than the range that could be due to errors in depth conversion or fault interpretation. The data are presented with error bars in Fig. 9d to illustrate this point, and show that typical errors are of the order of ±2 to 3°.

It is apparent from Fig. 9a and Table 3 that the faults from the Ormen Lange case study exhibit a range of dip angles that is generally towards the lower end of the total range of the combined dataset. There is a shift of approximately 10−15° compared to those from the Gjallar Ridge survey. From a comparison of wireline log characteristics, the lithology of the deformed Brygge and Kai Formations is similar in both areas, but the faults in Ormen Lange are buried to significantly greater depths than those in the Gjallar Ridge case study area, and this is suggested as an explanation of this bulk shift to lower dip values.

Some previous studies of polygonal fault systems have suggested that there is an azimuthal dependence of fault plane dip for

example in the case of the Late Cretaceous polygonal faults of the Møre Basin (Stuevold et al., 2003). To investigate this possibility, we plotted dip against fault plane strike measured at maps of the A/CT reflection for both case studies but no relationship was found (Fig. 10a). We examined the distribution of faults with contrasting dip values for segment 'a' (above the A/CT reflection), but could find no relationship between fault plane dip magnitude and location: there was no clustering of fault planes with relatively higher dips, nor was there any distinct zonation of higher or lower dips. We plotted fault plane dip against maximum throw, but again, observed no systematic relationship.

In summary, the large range in fault plane dips observed for segments 'a' and 'b' in both areas appears to be a scatter that does not correlate to strike, maximum throw or position in the survey area. Since the lateral continuity of seismic reflections in each survey area is very high, this suggests that any marked lithological variations are only likely on the scale of tens of kilometres. The random distribution and interspersal of fault segments with high and low dips indicates that this scatter cannot be related to any obvious lithological variation.

## 6. Discussion

### 6.1. Fault plane dip reduction and diagenesis

It is clear from the data presented in Figs. 4, 5, 7 and 9 and Table 3 that the dip of the polygonal faults systematically shallows across the A/CT reflection in the majority of cases. The abrupt nature of this shallowing of dip is seen on the seismic profiles to
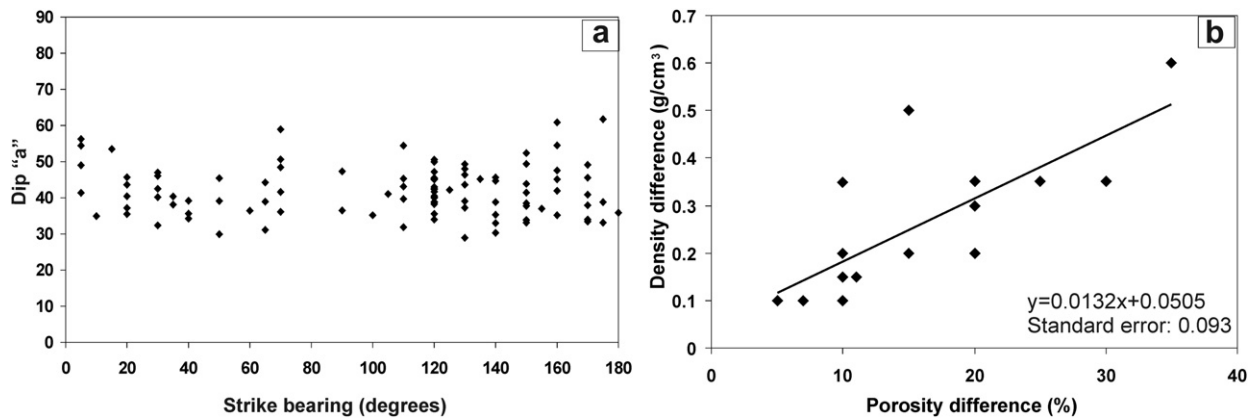
**Table 3**
Ranges of the dip angles for the fault segments above the A/CT reflection (dip "a") and below it (dip "b") for the two study areas. Corresponding average values are also shown.

| Survey area | No. faults measured | Dip above A/CT | | Dip below A/CT | |
|---|---|---|---|---|---|
| | | Range | Average | Range | Average |
| Gjallar Ridge | 387 | 41−74 | 54 | 26−58 | 43 |
| Ormen Lange | 100 | 29−62 | 42 | 19−40 | 29 |

**Fig. 10.** (a) Crossplot of dip "a" versus strike showing that no correlation exists between the magnitude of the dip angle and orientation of the faults in the Ormen Lange survey area. (b) Crossplot of porosity difference versus density difference across the A/CT boundaries for the ODP sites listed in Table 5.

coincide almost exactly with the A/CT reflection, suggesting that the two observations are related. This part of the discussion therefore attempts to address the key question as to why the polygonal faults change dip as they cross the A/CT boundary.

An abrupt change of dip could potentially be explained in two contrasting ways: (1) due to some original lithological layering leading to propagation at originally different angles and refraction at the boundary (c.f. Peacock and Zhang, 1994; Schöpfer et al., 2007), or (2) to a compactional flattening of the original fault plane dip (Jones and Addis, 1984). We can reject the first explanation for the simple reason that the diagenesis results in a denser, more cemented sedimentary lithology below the diagenetic front, in contrast with the unlithified high porosity precursor biosiliceous ooze prior to diagenesis. Sediments rich in opal-A have very low shear strength (e.g. Pittenger et al., 1989), whereas the cementation that occurs during opal-A to opal-CT transformation causes a distinct increase in the shear strength (Bjørlykke and Høeg, 1997). In known examples of fault refraction (Schöpfer et al., 2007 and references therein), the fault traces observed in cross-section have steeper dipping segments in the strong layers and shallower dipping segments in the weak ones. This has either been attributed to different modes of fracturing (tensile versus shear) as a function of lithology (e.g. Ferrill and Morris, 2003) or to different friction coefficients within the interbedded lithologies (e.g. Mandl, 2000). Thus, the observed reduction of dip at the A/CT boundary is the opposite of what would be predicted from a Mohr–Coulomb analysis.

The alternative interpretation for the reduction of dip is that the original fault plane dip has been substantially modified by later compaction. Strong support for this interpretation comes from the large body of porosity data from biosiliceous sediments that have undergone diagenesis obtained by the Ocean Drilling Programme (ODP). From these data, and from field evidence, it is now well known that the opal-A to opal-CT diagenesis coincides with an important decrease in porosity (e.g. Compton, 1991; Chaika and Dvorkin, 2000; Meadows and Davies, 2008). It is common to find that porosity values in biosiliceous oozes are high from the time of deposition and only gradually decrease with depth to the point where the sediment undergoes the diagenetic transformation, whereupon the porosity drops by as much as 20–30%.

In the Gjallar Ridge case study area, we are able to estimate the magnitude of the porosity reduction across the opal-A to opal-CT boundary from a combination of the density log from well 6704/12-1 located in the survey area and from physical property and lithological data from ODP Site 642, located some 50 km from the survey area (Eldholm et al., 1987) (location in Fig. 2a). At this location, the porosity of the opal-A rich sediments, averaged for about 50 m above the location of the A/CT boundary, is 80%, and within the opal-CT rich interval below is 70%. From the available density log of the well 6704/12-1 (Fig. 4a), we extracted the bulk density values in the sediments above and below the A/CT boundary. The average values are 1.3 and 1.55 g/cm$^3$, respectively for the intervals directly above and below the A/CT boundary. This abrupt increase of bulk density is known from ODP drilling to correspond to a reduction in porosity. We compiled a set of density values from ODP sources for boreholes that cross the A/CT boundary with measured porosity differences above and below it (Fig. 10b and Table 4). This plot is highly scattered, but nonetheless shows a crude correlation between the change in bulk density and the porosity change across the A/CT boundary. From the trend line, it can be seen that a density difference of 0.25 g/cm$^3$, observed locally in the well 6704/12-1 corresponds to a porosity change of 15%, which is comparable to that recorded by direct measurement in Site 642 (Table 5).

The compaction strain resulting from the diagenetic change can be calculated directly from the change in porosity across the A/CT boundary (Meadows and Davies, 2008). Here, we make the initial assumption that all the porosity change is expressed in a 1-D consolidation, and hence is expressed as a vertical strain. From this assumption, we define the compaction strain ($E_z$) as the ratio of the final solid thickness to the original solid thickness of a column of sediments. Technically, $E_z$ is equivalent to the stretch, which is one measure of strain (Twiss and Moores, 1992); however, in his paper $E_z$ will be referred to as compaction strain. $E_z$ is also the inverse of the decompaction number ($D$) of Perrier and Quiblier (1974):

$$E_z = \frac{1}{D} = \frac{h_1}{h_0} = \frac{1 - \phi_0}{1 - \phi_1},\qquad(1)$$

where $h_0$ = the initial solid thickness; $h_1$ = the final solid thickness; $\phi_0$ = initial porosity (porosity above the A/CT boundary or porosity 'a'); $\phi_1$ = final porosity (porosity above the A/CT boundary or porosity 'b').

**Table 4**
The parameters of the regression lines in Fig. 13b. The correlation coefficients between the two sets of values (dip "a" and compaction strain) and the average compaction strain values for both study areas.

| Survey area | Slope (m) | B (y-intercept) | Correlation coefficient (Pearson) | Average compaction strain |
|---|---|---|---|---|
| Gjallar Ridge | −0.0237 | 1.9807 | −0.74 | 0.7 |
| Ormen Lange | −0.0154 | 1.2693 | −0.8 | 0.6 |

**Table 5**
Variation of the porosity (%) and bulk density (g/cm³) of the opal-A ("a") and opal-CT ("b") sediment for several ODP/DSPD sites that have drilled the A/CT diagenetic boundary. Both porosity and bulk density values presented in this table have been averaged for 50 m above and below the A/CT boundary, based on the data provided by the ODP/DSDP Initial Reports (http://www-odp.tamu.edu).

| ODP/DSDP Leg | Site | Porosity "a" | Porosity "b" | Bulk density "a" | Bulk density "b" |
|---|---|---|---|---|---|
| ODP 104 | 642 | 80 | 70 | 1.35 | 1.70 |
| ODP 104 | 643 | 80 | 60 | 1.40 | 1.60 |
| ODP 121 | 752 | 55 | 30 | 1.85 | 2.20 |
| ODP 150 | 902 | 60 | 40 | 1.80 | 2.10 |
| ODP 150 | 904 | 60 | 50 | 1.80 | 1.90 |
| ODP 188 | 1165 | 55 | 45 | 1.70 | 1.90 |
| ODP 189 | 1172 | 63 | 52 | 1.55 | 1.70 |
| ODP 113 | 696 | 75 | 40 | 1.50 | 2.10 |
| ODP 178 | 1075 | 55 | 45 | 1.70 | 1.90 |
| ODP 127 | 794 | 85 | 70 | 1.20 | 1.70 |
| ODP 127 | 795 | 80 | 60 | 1.45 | 1.80 |
| ODP 105 | 647 | 80 | 50 | 1.45 | 1.80 |
| ODP 198 | 1207 | 65 | 58 | 1.70 | 1.80 |
| DSDP 95 | 612 | 60 | 45 | 1.60 | 1.80 |
| DSDP 95 | 613 | 55 | 45 | 1.65 | 1.75 |
| DSDP 47 | 397 | 45 | 40 | 1.90 | 2.00 |
| ODP 201 | 1225 | 75 | 65 | 1.45 | 1.60 |
| ODP 113 | 689 | 58 | 48 | 1.80 | 2.00 |
| ODP 138 | 847 | 75 | 65 | 1.40 | 1.60 |

The porosity is expressed as a fraction of sediment that is made up of pore space:

$$\phi = \frac{h_v}{h_t}, \tag{2}$$

where $h_v$ = the thickness of the pore spaces of a column of sediment; and $h_t$ = the total thickness of the sediment column.

The thickness of a solid fraction ($h_s$) of the sediment is:

$$h_s = h_t - h_v. \tag{3}$$

After the substitution of Eq. (3) into Eq. (2), the thickness of the solid fraction becomes:

$$h_s = h_t(1 - \phi). \tag{4}$$

During the diagenesis, we assume that the 'solid thickness' of the solid fraction remains constant, which is valid provided the phase change occurs only on a local scale (Perrier and Quiblier, 1974). In our case, the dissolution − precipitation reactions involved in converting opal-A to opal-C/T are generally considered to operate on a grain scale, without mass transfer over distances of more than a few millimetres (Hein et al., 1978; Davies, 2005) i.e. at a much smaller scale than the solid thicknesses considered (hundreds of meters). Thus we can consider that the final solid thickness equals the initial solid thickness (i.e. there is no significant mass transfer):

$$h_1(1 - \phi_1) = h_0(1 - \phi_0). \tag{5}$$

Using the values of porosity change from Site 642, we obtain a compaction strain of 0.66, or using the larger porosity change of 15% from the density log response of well 6704/12-1, and a pre-diagenetic porosity of 80%, we obtain a compaction strain of 0.57. These two values probably represent reasonable upper and lower bounds for the compaction strain in the Gjallar Ridge case study area, due to silica diagenesis, with the assumptions stated above.

### 6.2. Compaction strain from fault plane flattening

If a fault plane is considered as a linear marker that flattens with vertical compaction (e.g. Davison, 1987), its dip angle changes from $\theta_0$ to $\theta_1$ as illustrated in Fig. 11. From simple trigonometry, the ratio of the final solid thickness to the initial solid thickness can be directly related to the change in dip angle:

$$\frac{h_1}{h_0} = \frac{\tan \theta_1}{\tan \theta_0}, \tag{6}$$

where $\theta_0$ = initial dip angle and $\theta_1$ = final dip angle. If a case could be made that the polygonal faults in the study areas were planar prior to the diagenesis of the opal-A fraction of the biosiliceous sediment, then the compaction strain could be calculated from the change in fault dip using Eq. (6). Polygonal faults are often described as being planar to gently listric (e.g. Cartwright and Lonergan, 1996; Lonergan et al., 1998; Stuevold et al., 2003). In order to quantify this geometry we measured fault plane dips for a selection of faults that occur in the interval above the A/CT boundary in the Gjallar Ridge case study area. These data show that polygonal fault planes are curviplanar with a dip variation of less than 20° for vertical distances of 300−500 m within the biosiliceous, opal-A rich, Brygge and Kai Formations (Fig. 12). It is also well established that polygonal faults form during early burial (Cartwright et al., 2003; Gay et al., 2004), perhaps at depths of burial as shallow as 50 m or so. In contrast, diagenetic transformation from opal-A to opal-CT is thought to occur at temperatures in the range 20−50 °C (Hein et al., 1978), which for a reasonable assumed temperature gradient (Brekke, 2000) of 50 °C per kilometre would equate to a burial depth of approximately 400 m. This suggests that the polygonal faults predated the onset of diagenetic transformation of the opaline silica in the deformed interval, and hence further supports the view that the faults can be used as pre-diagenetic markers to quantify the compactional effects of diagenesis.

Based on the data in Fig. 9, we used Eq. (6) to calculate compaction strain values for all the faults in the Gjallar Ridge survey area, which gave a normal distribution with a mean value of 0.7 (Fig. 13a and Table 2). The scatter in the compaction strain values can be equated to the scatter in the fault dip values above the A/CT boundary. By plotting the dip value 'a' against the compaction strain, it can be seen that the steeper the original fault plane dip, the greater is the compaction strain calculated from the dip changes across the A/CT boundary (Fig. 13b). The mean compaction strain calculated using this method (0.7) thus closely approximates the value bounds derived from the change in porosity and bulk density (0.57−0.66).

The closely comparable values for the compaction strain obtained from the porosity/density measurements and from the reduction in fault plane dip argues strongly that silica diagenesis in this region offshore Norway resulted in a significant and abrupt
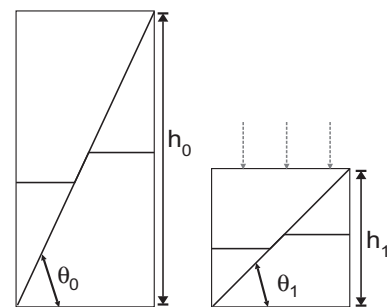


**Fig. 11.** Schematic representation of the flattening of a fault plane with vertical compaction. Note that the dip angle of the fault changes from $\theta_0$ (initial dip angle) to $\theta_1$ (final dip angle). $h_0$ and $h_1$ represent the initial and final solid thickness of a volume of sediments, respectively.
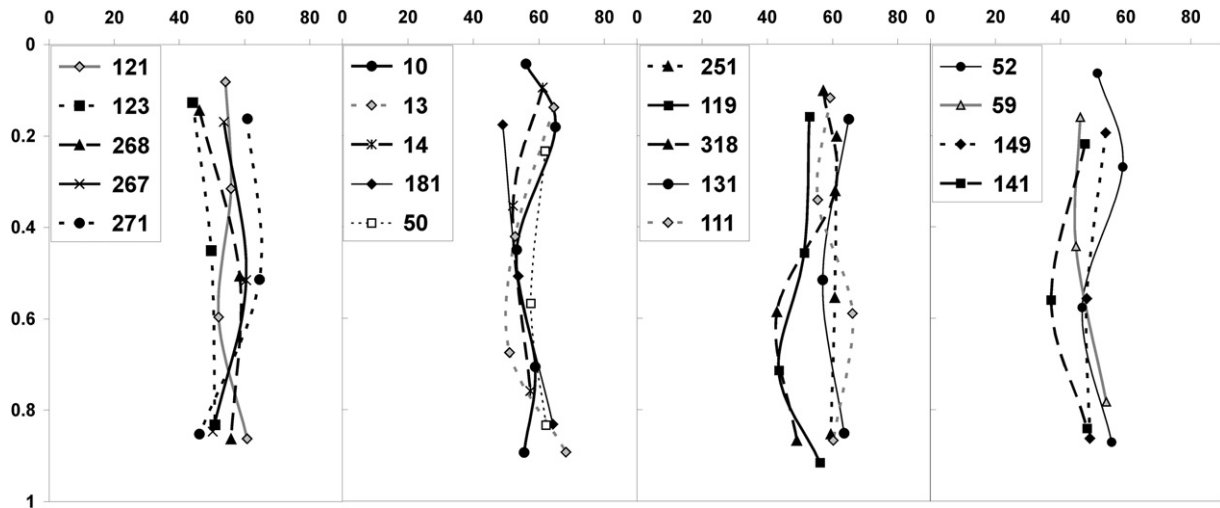
**Fig. 12.** Dip variation (abscissa) with normalised depth (ordinate) for a selection of faults that occur in the interval above the A/CT reflection in the Gjallar Ridge study area. The change in dips of up to 20° is not systematical over 300–500 m of the vertical height.

vertical consolidation. Redwine (1981) suggested the consolidation could be triggered by loss of grain-to-grain contact stresses upon the dissolution of opal-A skeletal particles. There is no need to invoke significant lateral strains (e.g. Cartwright and Lonergan, 1996) simply because the two independent methods for vertical strain computation provide comparable values. If there was significant lateral (horizontal) strain at the grain scale due to the collapse of porosity, this would have resulted in a mismatch between the two sets of values, with a lesser degree of vertical consolidation implying the need for a smaller fault plane dip reduction.

The results above demonstrate that the vertical compaction strain due to silica diagenesis can be predicted to reasonable accuracy in areas where there are no direct measurements of porosity or density, simply from the observation of reduction of fault plane dip. This technique can potentially be applied in many areas of the world where sedimentary layers that host polygonal fault systems have also been subject to silica diagenesis, such as offshore West Africa, the Blake Plateau, offshore Ireland and offshore NW Australia (Cartwright and Dewhurst, 1998). This technique does not yield absolute porosity value predictions, because similar compaction strains can be obtained for very different initial and final porosity values (Meadows and Davies,

2008). Much further work is required for a direct prediction of porosity prior to and after this diagenetic transformation, because initial porosity and porosity reduction are likely to vary according to the specific concentration of silica in the original sediment, in addition to the presence of secondary minerals (clays and carbonates) (Nobes et al., 1992).

### 6.3. Fault growth during silica diagenesis

The preceding discussion has argued the case that during the transformation of opal-A to opal-CT results in a porosity collapse and a vertical consolidation that passively rotates dipping markers (fault planes) into shallower dip angles. We now conclude the discussion by considering what impact this dip reduction should have on continued fault growth, and what we can infer regarding the actual growth of the polygonal faults in the two case study areas.

The dip measurements presented in Fig. 9a, b show that reduction of dip across the A/CT boundary is typically 15–20°, but in many cases of steeper initial dip, this can exceed 25°. It was also noted above that the cementation of opal-CT results in an increase in shear strength from the opal-A rich unconsolidated sediment to the opal-CT, cemented sediment (Pittenger et al., 1989; Bjørlykke
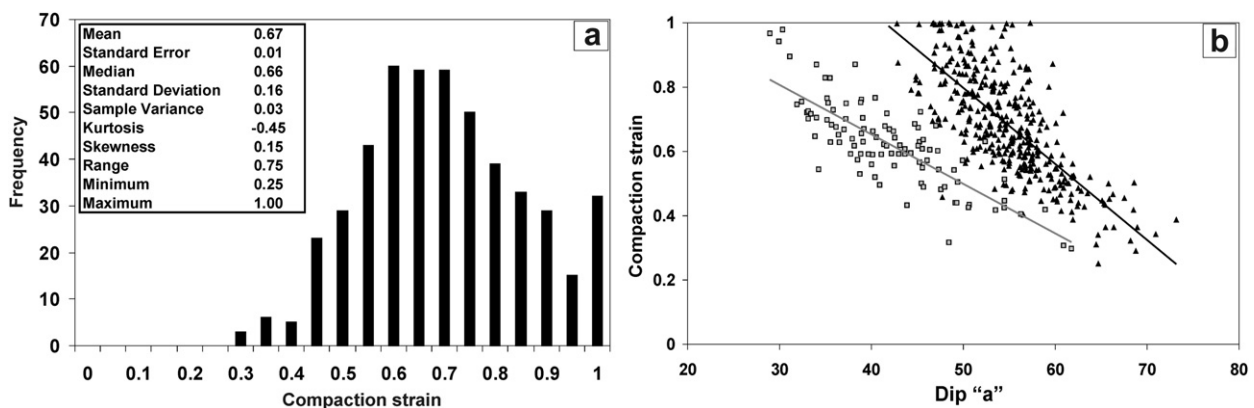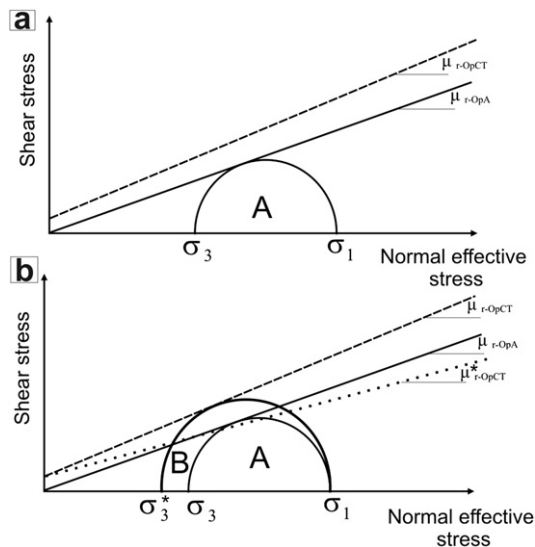


**Fig. 13.** (a) Histogram showing the frequency of the compaction strain values for both surveys. Corresponding descriptive statistics are also shown. (b) Crossplot of the compaction strain values versus dip "a" values for the faults in Gjallar Ridge area (filled triangles) and Ormen Lange (open squares). The regression parameters and correlation coefficients for the two sets of values are presented in Table 4.

and Høeg, 1997). There are few direct measurements of shear strength of opal-CT sediments, so we represent this change schematically in a Mohr construction in Fig. 14. This construction suggests that the in situ stress state prior to diagenesis necessary to maintain active slip given a coefficient of friction appropriate for opal-A rich sediment ($\mu_{\text{r-OpA}}$) would be insufficient to permit slip at the same burial depth for a material with a higher shear strength ($\mu_{\text{r-OpCT}}$). When it is considered that the fault plane shallows by approximately 20° across the diagenetic front, it is even less likely that slip should occur after diagenesis. It follows from this, that in order to maintain active slip on a fault that has been rotated by this magnitude, a substantial reduction in friction coefficient and/or a substantial increase in differential effective stress (by reducing the least confining stress) are required.

Since silica diagenesis is known to result in the expulsion of large relative volumes of water (Jones and Segnit, 1971; Volpi et al., 2003; Davies and Cartwright, 2007), one possible mechanism for obtaining a reduced value for residual frictional strength of the fault zone is by dilation through pore fluid expulsion, similar to that invoked to explain fluid flow along thrust faults in accretionary prisms (e.g. Byrne et al., 1993; Cobbold and Rodrigues, 2007). Alternatively, it may be that the fault zone never becomes cemented by opal-CT, because of the different micromechanical conditions extant on an active fault zone as opposed to those experienced by the intact sediment of the surrounding fault blocks. Reduction in least confining stress would not normally be predicted by classical soil mechanics under confined loading, but in the situation prevalent here, where active dissolution was occurring during diagenesis, significant reductions in the least principle stress may be predicted (Shin et al., 2008). These speculative suggestions need further testing, but collectively argue that deviations from classical Mohr−Coulomb behaviour may be expected during the combined processes of diagenesis and porosity collapse, and may indeed be sufficient to promote continued fault growth.

There can be little doubt that diagenesis and porosity collapse leading to fault plane flattening did not adversely impact the continued accumulation of displacement on the polygonal faults in the study areas, and more generally in the Møre and Vøring Basins, offshore Norway. The plots of throw variation with depth measured from the two case study areas all show that displacement accumulated after the upward migration of the diagenetic had effectively ceased (Fig. 8), sometime in the late Pliocene. This is consistent with the observation that the A/CT reflection is near parallel to the base of the Naust (Late Pliocene) Formation in this area, supporting Brekke (2000) suggestion of an arrested development of the diagenesis of opal-A to opal-CT at about this time. Cessation of the upward migration of the reaction front does not of course imply necessarily that all silica diagenesis ceased at this time, but given that opal-A is almost entirely converted at the reaction front, cessation of migration of the front is equivalent to a effective halt to any further porosity collapse mechanism or other substantial change in physical properties in the lower interval. The accumulation of further displacement after this point in time must therefore have occurred under the conditions stipulated in the schematic Mohr construction of Fig. 14, but without the probable involvement of large pore fluid flux or dissolution-related change in confining stress.

## 7. Conclusions

1. Polygonal fault planes within the Brygge and Kai Formations, of the Møre and Vøring Basins exhibit an unusual planar segmented fault plane geometry, whereby the planar segments dip more steeply in the opal-A rich biosiliceous mudstones than in the underlying opal-CT rich interval.

2. The change in dip in the fault plane segments occurs at or close to the diagenetic boundary between the opal-A rich and the opal-CT rich biosiliceous mudstones. The dip above the reaction boundary is widely scattered from approximately 40 to 70°, and below the boundary ranges from approximately 30° to 50°. The dip above correlates well with the dip below the boundary, for the around 500 fault planes measured in this study. There is no obvious correlation of the fault plane dip with lithology or structural parameters.

3. The magnitude of the dip reduction across the opal-A to opal-CT reaction boundary is approximately 15−20°.

4. Estimates of the compaction strain based on porosity and density measurements from calibration wells are 0.57−0.66. This equates well with the mean vertical compaction strain calculated from the change of fault plane dip, assuming the fault planes were planar markers prior to diagenesis. This equivalence suggests that the fault planes were passively rotated into shallower dips as a result of diagenesis.

5. The rotation of fault planes as a result of diagenesis offers a new method for estimating the porosity reduction due to silica diagenesis.

6. The faults continued to grow after diagenesis had effectively ceased, and as a result the opal-A/CT reflection is systematically offset by a lesser amount than the throw on the true stratal markers. Continued growth occurred in spite of changes in physical properties such as an increase in shear strength, and in spite of a reduction in fault plane dip. This post-diagenetic phase of growth cannot be explained mechanically at present.

**Fig. 14.** (a). Mohr−Coulomb failure envelopes for the same sediment before diagenesis (continuous line) and after diagenesis (dashed line). $\mu_{\text{r-OpA}}$ is the coefficient of friction for opal-A rich sediment and $\mu_{\text{r-OpCT}}$ is the coefficient of friction for opal-CT rich sediment. $\sigma_1$ and $\sigma_3$ are the maximum and minimum principal stresses, respectively. The in situ stress state prior to diagenesis (circle A), necessary to maintain active slip, would be insufficient to permit slip at the same burial depth for a material with a higher shear strength (opal-CT). (b). Shear failure could occur by decreasing the friction angle to $\mu_{\text{r-OpCT}}^{*}$ (the shear failure envelope is represented by the dotted black line) while maintaining the same stress state (circle A) or by reducing the minimum normal stress to $\sigma_3^{*}$ (stress circle B).

## Appendix 1

Estimated percentage of throw accumulated on the adjacent stratigraphic markers (above and below the A/CT reflection) after the diagenesis ceased. The values correspond to the faults presented in Fig. 8 and were calculated using the formula:

$$T_{ab} = \frac{T_{ab} - T_{A/CT}}{T_{ab}} \times 100,$$

where $T_{ab}$ is the throw on the stratigraphic marker adjacent to the A/CT reflection (either above or below it) and $T_{A/CT}$ is the throw on the A/CT reflection.

| Survey area | Fault no. | Percentage of throw (%) | |
|---|---|---|---|
| | | Stratigraphic marker above A/CT | Stratigraphic marker below A/CT |
| Gjallar Ridge | 8 | 19 | 35 |
| | 6 | 31 | 31 |
| | 5 | 0 | 35 |
| | 117 | 74 | 70 |
| | 129 | 54 | 33 |
| | 147 | 50 | 39 |
| | 87 | 58 | 62 |
| | 219 | 43 | 33 |
| | 246 | 20 | 0 |
| | 68 | 53 | 56 |
| | 344 | 63 | 57 |
| | 69 | 60 | 71 |
| | 301 | 25 | 45 |
| | 88 | 33 | 50 |
| | 309 | 22 | 53 |
| Ormen Lange | 21 | 13 | 28 |
| | 24 | 39 | 26 |
| | 59 | 17 | 33 |
| | 76 | 53 | 27 |

## References

Amante, C., Eakins, B.W., 2008. ETOPO1 1 Arc-Minute Global Relief Model: Procedures, Data Sources and Analysis. National Geophysical Data Center, NESDIS, NOAA, U.S. Department of Commerce, Boulder, CO.

Audet, D.M., Fowler, A.C., 1992. A mathematical model for compaction in sedimentary basins. Geophysical Journal International 110 (3), 577–590.

Baudon, C., Cartwright, J., 2008. The kinematics of reactivation of normal faults using high resolution throw mapping. Journal of Structural Geology 30 (8), 1072–1084.

Bayer, U., Wetzel, A., 1989. Compactional behavior of fine-grained sediments – examples from Deep Sea Drilling Project cores. International Journal of Earth Sciences 78 (3), 807–819.

Berndt, C., Bünz, S., Clayton, T., Mienert, J., Saunders, M., 2004. Seismic character of bottom simulating reflectors: examples from the mid-Norwegian margin. Marine and Petroleum Geology 21 (6), 723–733.

Berndt, C., Bünz, S., Mienert, J., 2003. Polygonal fault systems on the mid-Norwegian margin: a long-term source for fluid flow. Geological Society, London, Special Publication 216, 283–290.

Bethke, C.M., Corbet, T.F., 1988. Linear and nonlinear solutions for one-dimensional compaction flow in sedimentary basins. Water Resources Research 24 (3), 461–467.

Bjørlykke, K., Høeg, K., 1997. Effects of burial diagenesis on stresses, compaction and fluid flow in sedimentary basins. Marine and Petroleum Geology 14 (3), 267–276.

Blystad, P., Brekke, H., Færseth, R.B., Larsen, B.T., Skogseid, J., Tørudbakken, B., 1995. Structural elements of the Norwegian continental shelf. Part II: the Norwegian Sea region. Norwegian Petroleum Directory Bulletin 6.

Bohrmann, G., Spieß, V., Hinze, H., Kuhn, G., 1992. Reflector 'Pc' a prominent feature in the Maud Rise sediment sequence (eastern Weddell Sea): occurrence, regional distribution and implications to silica diagenesis. Marine Geology 106 (1–2), 69–87.

Brekke, H., 2000. The tectonic evolution of the Norwegian Sea continental margin with emphasis on the Voring and More Basins. Geological Society, London, Special Publication 167, 327–378.

Brekke, H., Riis, F., 1987. Tectonic and basin evolution of the Norwegian shelf between 62° N and 72° N. Norsk Geologisk Tidsskrift 67, 295–321.

Bryn, P., Berg, K., Stoker, M., Haflidason, H., Solheim, A., 2005. Contourites and their relevance for mass wasting along the mid-Norwegian margin. Marine and Petroleum Geology 22 (1–2), 85–96.

Brown, A., 2004. Interpretation of Three-Dimensional Seismic Data, sixth ed. American Association of Petroleum Geologists Memoir.

Byrne, T., Maltman, A., Stephenson, E., Soh, W., Knipe, R., 1993. Deformation structures and fluid flow in the toe region of the Nankai accretionary prism. In: Hill, I.A., Taira, A., Firth, J.V., et al. (Eds.), Proceeding of the ODP, Scientific Results, 131. Ocean Drilling Program, College Station, TX, pp. 83–101. doi:10.2973/odp.proc.sr.131.107.1993.

Cartwright, J.A., 1994. Episodic basin-wide fluid expulsion from geopressured shale sequences in the North Sea Basin. Geology 22 (5), 447–450.

Cartwright, J.A., 1996. Polygonal fault systems: a new type of fault structure revealed by 3D seismic data from the North Sea Basin. American Association of Petroleum Geologists Studies in Geology 42, 225–230.

Cartwright, J.A., 2007. The impact of 3D seismic data on the understanding of compaction, fluid flow and diagenesis in sedimentary basins. Journal of the Geological Society 164, 881–893.

Cartwright, J.A., Bouroullec, R., James, D., Johnson, H.D., 1998. Polycyclic motion history of some Gulf Coast growth faults from high-resolution displacement analysis. Geology 26 (9), 819–822.

Cartwright, J.A., Dewhurst, D.N., 1998. Layer-bound compaction faults in fine-grained sediments. Bulletin of the Geological Society of America 110 (10), 1242–1257.

Cartwright, J.A., James, D., Bolton, A., 2003. The genesis of polygonal fault systems: a review. In: Van Rensbergen, P., Hillis, R.R., Maltman, A.J., Morley, C.K. (Eds.), Subsurface Sediment Mobilization. Geological Society, London, Special Publications, vol. 216, pp. 223–243.

Cartwright, J.A., Lonergan, L., 1996. Volumetric contraction during the compaction of mudrocks: a mechanism for the development of regional-scale polygonal fault systems. Basin Research 8 (2), 183–193.

Chaika, C., Dvorkin, J., 1997. Ultrasonic velocities of opaline rocks undergoing silica diagenesis. Geophysics Research Letters 24 (16), 2039–2042.

Chaika, C., Dvorkin, J., 2000. Porosity reduction during diagenesis of diatomaceous rocks. American Association of Petroleum Geologists Bulletin 84 (8), 1173–1184.

Cobbold, P.R., Rodrigues, N., 2007. Seepage forces, important factors in the formation of horizontal hydraulic fractures and bedding-parallel fibrous veins ('beef' and 'cone-in-cone'). Geofluids 7 (3), 313–322.

Compton, J.S., 1991. Porosity reduction and burial history of siliceous rocks from the Monterey and Sisquoc Formations, Point Pedernales area, California. Geological Society of America Bulletin 103 (5), 625–636.

Craig, J., 1987. The structure of the Llangranog Lineament, West Wales: a Caledonian transpression zone. Geological Journal 22 (S1), 167–181.

Davies, R.J., 2005. Differential compaction and subsidence in sedimentary basins due to silica diagenesis: a case study. Bulletin of the Geological Society of America 117 (9–10), 1146–1155.

Davies, R.J., Cartwright, J., 2002. A fossilized opal-A to opal C/T transformation on the northeast Atlantic margin: support for a significantly elevated palaeogeothermal gradient during the Neogene? Basin Research 14 (4), 467–486.

Davies, R.J., Cartwright, J.A., 2007. Kilometer-scale chemical reaction boundary patterns and deformation in sedimentary rocks. Earth and Planetary Science Letters 262 (1–2), 125–137.

Davies, R., Cartwright, J., Rana, J., 1999. Giant hummocks in deep-water marine sediments: evidence for large scale differential compaction and density inversion during early burial. Geology 27 (10), 907–910.

Davies, R.J., Goulty, N.R., Meadows, D., 2008. Fluid flow due to the advance of basin-scale silica reaction zones. Bulletin of the Geological Society of America 120 (1–2), 195–206.

Davies, R.J., Ireland, M., Cartwright, J., 2009. Differential compaction due to the irregular topology of a diagenetic reaction boundary: a new mechanism for the formation of polygonal faults. Basin Research 21 (3), 354–359.

Davison, I., 1987. Normal fault geometry related to sediment compaction and burial. Journal of Structural Geology 9 (4), 393–401.

Dewhurst, D.N., Cartwright, J.A., Lonergan, L., 1999. The development of polygonal fault systems by syneresis of colloidal sediments. Marine and Petroleum Geology 16 (8), 793–810.

Doré, A.G., Lundin, E.R., 1996. Cenozoic compressional structures of the NE Atlantic margin: nature, origin and potential significance for hydrocarbon exploration. Petroleum Geoscience 2, 299–311.

Eldholm, O., 1991. Magmatic–tectonic evolution of a volcanic rifted margin. Marine Geology 102, 42–61.

Eldholm, O., Thiede, J., Taylor, E., et al., 1987. Proceedings of ODP. Initial reports, 104. Ocean Drilling Program, College Station, TX. doi:10.2973/odp.proc.ir.104.1987.

Ferrill, D., Morris, A., 2003. Dilational normal faults. Journal of Structural Geology 25 (2), 183–196.

Gay, A., Berndt, C., 2007. Cessation/reactivation of polygonal faulting and effects on fluid flow in the Vøring Basin, Norwegian margin. Journal of the Geological Society 164 (1), 129–141.

Gay, A., Lopez, M., Cochonat, P., Sermondadaz, G., 2004. Polygonal faults-furrows system related to early stages of compaction − upper Miocene to recent sediments of the Lower Congo Basin. Basin Research 16 (1), 101–116.

Gómez, M., Vergés, J., 2005. Quantifying the contribution of tectonics vs. differential compaction in the development of domes along the mid-Norwegian Atlantic margin. Basin Research 17, 289–310.

Goulty, N.R., 2001. Polygonal fault networks in fine-grained sediments; an alternative to the syneresis mechanism. First Break 19 (2), 69–73.

Goulty, N.R., 2002. Mechanics of layer-bound polygonal faulting in fine-grained sediments. Journal of the Geological Society 159 (3), 239–246.

Goulty, N., Swarbrick, R., 2005. Development of polygonal fault systems: a test of hypotheses. Journal of the Geological Society 162 (4), 587–590.

Hamilton, E.L., 1976. Shear-wave velocity versus depth in marine sediments: a review. Geophysics 41 (5), 985–996.

Hansen, J.P.V., Cartwright, J.A., Huuse, M., Clausen, O.R., 2005. 3D seismic expression of fluid migration and mud remobilization on the Gjallar Ridge, offshore mid-Norway. Basin Research 17 (1), 123–139.

Hein, J.R., Scholl, D.W., Barron, J.A., Jones, M.G., Miller, J., 1978. Diagenesis of late Cenozoic diatomaceous deposits and formation of the bottom simulating reflector in the southern Bering Sea. Sedimentology 25, 155–181.

Henriet, J.P., De Batist, M., Verschuren, M., 1991. Early fracturing of Palaeogene clays, southernmost North Sea: relevance to mechanisms of primary hydrocarbon migration. In: Generation, Accumulation, and Production of Europe's Hydrocarbons, pp. 217–227.

Hillier, R.D., Cosgrove, J.W., 2002. Core and seismic observations of overpressure related deformation within Eocene sediments of the Outer Moray Firth, UKCS. Petroleum Geoscience 8, 141–149.

Hjelstuen, B., 1997. Vøring Plateau diapir fields and their structural and depositional settings. Marine Geology 144 (1–3), 33–57.

Isaacs, C.M., 1981. Porosity reduction during diagenesis of the Monterey Formation, Santa Barbara coastal area, California. In: The Monterey Formation and Related Siliceous Rocks of California, pp. 257–271.

Jones, M.E., Addis, M.A., 1984. Volume change during sediment diagenesis and the development of growth faults. Marine and Petroleum Geology 1 (2), 118–122.

Jones, J.B., Segnit, E.R., 1971. The nature of opal. I. Nomenclature and constituent phases. Geological Society of Australia Journal 68, 56–68.

Kastner, M., Keene, J.B., Gieskes, J.M., 1977. Diagenesis of siliceous oozes-I. Chemical controls on the rate of opal-A to opal-CT transformation − an experimental study. Geochimica et Cosmochimica Acta 41 (8), 1041–1059.

Lonergan, L., Cartwright, J., Jolly, R., 1998. The geometry of polygonal fault systems in Tertiary mudrocks of the North Sea. Journal of Structural Geology 20 (5), 529–548.

Mandl, G., 2000. Faulting in Brittle Rocks: an Introduction to the Mechanics of Tectonic Faults. Springer-Verlag, New York, 434 pp.

Mansfield, C.S., Cartwright, J.A., 1996. High resolution fault displacement mapping from three-dimensional seismic data: evidence for dip linkage during fault growth. Journal of Structural Geology 18 (2–3), 249–263.

Meadows, D., Davies, R.J., 2008. Predicting porosity reduction due to silica diagenesis using seismic reflection data. Marine and Petroleum Geology. doi:10.1016/j.marpetgeo.2008.09.006.

Muraoka, H., Kamata, H., 1983. Displacement distribution along minor fault traces. Journal of Structural Geology 5 (5), 483–495.

Murata, K.J., Larson, R.R., 1975. Diagenesis of Miocene siliceous shales, Temblor Range, California. Journal of Research of the US Geological Survey 3 (5), 553–566.

Nobes, D.C., Murray, R.W., Kuramoto, S., Pisciotto, K.A., Holler, P., 1992. Impact of silica diagenesis on physical property variations. In: Pisciotto, K.A., Ingle Jr., J.C., von Breymann, M.T., Barron, J., et al. (Eds.), Proceedings of ODP, Scientific

Results. Ocean Drilling Program, College Station, TX, pp. 3–31. doi:10.2973/odp. proc.sr.127128-1.111.1992. 127/128 (Pt. 1).

Parize, O., Beaudoin, B., 1988. Clastic dykes and sills from Numidian flysch (Sicily and Tunisia): sandy injection related to a high-density turbidity deposit. AAPG Bulletin 72 (8), 1018.

Peacock, D.C.P., Zhang, X., 1994. Field examples and numerical modeling of oversteps and bends along normal faults in cross-section. Tectonophysics 234, 147–167.

Perrier, R., Quiblier, J., 1974. Thickness changes in sedimentary layers during compaction history; methods for quantitative evaluation. AAPG Bulletin 58 (3), 507–520.

Pittenger, A., Taylor, E., Bryant, W.R., 1989. The influence of biogenic silica on the geotechnical stratigraphy of the Vøring Plateau, Norwegian Sea. In: Eldholm, O., Thiede, J., Taylor, E., et al. (Eds.), Proceedings of ODP, Scientific Results, 104. Ocean Drilling Program, College Station, TX, pp. 923–940.

Redwine, L., 1981. Hypothesis combining dilation, natural hydraulic fracturing, and dolomitization to explain petroleum reservoirs in Monterey shale, Santa Maria area, California. In: Garrison, R.E., Douglas, R.G. (Eds.), The Monterey Formation and Related Siliceous Rocks of California. Pacific Section, Society of Economic Paleontologists and Mineralogists, Los Angeles, pp. 221–248.

Rieke, H.H., Chilingarian, C.V., 1974. Compaction of Argillaceous Sediments. In: Developments in Sedimentology 16. Elsevier, Amsterdam.

Rokoengen, K., 1995. Upper Cenozoic stratigraphy on the mid-Norwegian continental shelf. Norsk Geologisk Tidsskrift 75 (2–3), 88–104.

Scheck-Wenderoth, M., Raum, T., Faleide, J.I., Mjelde, R., Horsfield, B., 2007. The transition from the continent to the ocean: a deeper view on the Norwegian margin. Journal of the Geological Society, London 164, 855–868.

Schöpfer, M.P.J., Childs, C., Walsh, J., Manzocchi, T., Koyi, H., 2007. Geometrical analysis of the refraction and segmentation of normal faults in periodically layered sequences. Journal of Structural Geology 29, 318–335.

Shelton, J.W., 1984. Listric normal faults; an illustrated summary. AAPG Bulletin 68 (7), 801–815.

Shin, H., Santamarina, J.C., Cartwright, J.A., 2008. Contraction-driven shear failure in compacting uncemented sediments. Geology 36, 931–934.

Skempton, A., 1981. Landmarks in early soil mechanics. In: Proceedings of the 7th European Conference on Soil Mechanics and Foundation Engineering 5, pp. 1–26.

Skogseid, J., Eldholm, O., 1989. Vøring Plateau continental margin: seismic interpretation, stratigraphy, and vertical movements. In: Proceedings of the Ocean Drilling Program, Scientific Results, vol. 104, pp. 993–1030.

Skogseid, J., Pedersen, T., Larsen, V.B., 1992. Vøring Basin: subsidence and tectonic evolution. In: Larsen, R., Brekke, M., Larsen, B.T., Talleraas, E. (Eds.), Structural and Tectonic Modelling and Its Application to Petroleum Geology. Norway Petroleum Society, vol. 1. Elsevier, Amsterdam, pp. 55–82.

Stuevold, L.M., Faerseth, R.B., Arnesen, L., Cartwright, J., Möller, N., 2003. Polygonal faults in the Ormen Lange Field, Møre Basin, offshore Mid Norway. Geological Society, London, Special Publications 216, 263–281.

Terzaghi, K., Peck, Ralph B., 1948. Soil Mechanics in Engineering Practice. John Wiley and Sons, New York.

Twiss, R.J., Moores, E.M., 1992. Structural Geology. W.H. Freeman and Company, New York, 532 pp.

Velde, B., 1996. Compaction trends of clay-rich deep sea sediments. Marine Geology 133, 193–201.

Volpi, V., Camerlenghi, A., Hillenbrand, C.D., Rebesco, M., Ivaldi, R., 2003. Effects of biogenic silica on sediment compaction and slope stability on the Pacific margin of the Antarctic Peninsula. Basin Research 15 (3), 339–363.

Walsh, J., Watterson, J., 1987. Displacement efficiency of faults and fractures: discussion. Journal of Structural Geology 9 (8), 1051–1052.

Watterson, J., Walsh, J., Nicol, A., Nell, P.A.R., Bretan, P.G., 2000. Geometry and origin of a polygonal fault system. Journal of the Geological Society 157 (1), 151–162.

Williams, L.A., Crerar, D.A., 1985. Silica diagenesis: II. General mechanisms. Journal of Sedimentary Petrology 55 (3), 312–321.